Measurement Report: Cloud condensation nuclei (CCN) activity in the South China Sea from shipborne observations during summer and winter of 2021: seasonal variation and anthropogenic influence.

Hengjia Ou[1], Mingfu Cai[2], Yongyun Zhang[1], Xue Ni[1], Baoling Liang[3], Qibin Sun[4,5], Shixin Mai[1], Cuizhi Sun[6], Shengzhen Zhou[1], Haichao Wang[1], Jiaren Sun[2], Jun Zhao[1]

[1]School of Atmospheric Sciences, Guangdong Province Key Laboratory for Climate Change and Natural Disaster Studies, Southern Marine Science and Engineering Guangdong Laboratory (Zhuhai), Sun Yat-sen University, Zhuhai, Guangdong 519082, China

[2]Guangdong Province Engineering Laboratory for Air Pollution Control, Guangdong Provincial Key Laboratory of Water and Air Pollution Control, South China Institute of Environmental Sciences, MEE, Guangzhou 510655, China

[3]Guangzhou Sub-branch of Guangdong Ecological and Environmental Monitoring Center, Guangzhou 510006, China

[4]Dongguan Meteorological Bureau, Dongguan, Guangdong, 523086, China

[5]Dongguan Engineering Technology Research Center of Urban Eco-Environmental Meteorology, Dongguan, Guangdong, 523086, China

[6]Southern Marine Science and Engineering Guangdong Laboratory (Zhuhai), Zhuhai, Guangdong 519082, China

Correspondence: Mingfu Cai (caimingfu@scies.org) and Jun Zhao (zhaojun23@mail.sysu.edu.cn)

Abstract

Understanding seasonal variations in cloud condensation nuclei (CCN) activity and the impact of anthropogenic emissions in marine environments is crucial for assessing climate change. This study presents findings from two shipborne observations conducted in the South China Sea (SCS) during the summer and winter of 2021. In summer, higher particle number concentrations but lower mass concentrations of non-refractory submicron particles (NR-PM_1) were observed, driven by Aitken mode particle dominance. In contrast, winter showed a more balanced distribution between Aitken and Accumulation mode particles. Summer particles were more hygroscopic, exhibiting higher activation ratios (ARs) at all supersaturation (SS) levels. Distinct air mass periods were identified: in summer, terrestrial air masses from Luzon ("Luzon" period), the Indochinese Peninsula ("Indochinese Peninsula" period), and marine air masses; in winter, periods were influenced by Mainland China ("Mainland China" period), a mix of Mainland China and marine air masses ("Mixed" period), and purely marine air masses. The "Luzon" period in summer exhibited the highest particle number concentration, especially in the Aitken mode, resulting in the highest CCN number concentration (N_{CCN}). Aerosol hygroscopicity was higher during the "Indochinese Peninsula" period compared to the "Luzon" period, leading to a higher bulk AR due to the combination of higher hygroscopicity and a greater fraction of accumulation mode particles. The "Mainland China" period in winter showed a high nitrate fraction in the NR-PM_1, but the inorganic fraction was similar to it in the "Luzon" period, resulting in comparable hygroscopicity at low SS to the "Luzon" period. However, smaller particle hygroscopicity was significantly lower in the "Mainland China" period compared to summer. The "Mixed" period in winter exhibited a higher fraction of accumulation mode particles, causing a higher bulk AR compared to the "Mainland China" period. Overall, summer terrestrial air masses increased Aitken particle and CCN concentrations, while winter terrestrial air masses led to a higher concentration of large particles and lower hygroscopicity of fine particles. CCN closure analysis, considering aerosol composition and mixing state, revealed that summer aerosol was primarily internally mixed, whereas smaller aerosol in winter was primarily externally mixed. The potential effect of undetected sea salt may lead to an underestimation of aerosol hygroscopicity in summer. This study highlights significant seasonal differences in aerosol properties and the impact of different types of terrestrial air masses on CCN activity in the SCS, contributing to our understanding of regional climate influences.

1.Introduction

Aerosols can act as cloud condensation nuclei (CCN), influencing cloud formation, lifespan, and albedo, thus indirectly impacting global radiative balance (Fletcher et al., 2011; Albrecht, 1989). The aerosol-cloud interaction currently represents the largest uncertainty in radiative forcing within climate models, ranging from -1.7 to -0.3 W m^{-2} (IPCC, 2021). This uncertainty can be attributed to the significant spatiotemporal variability in the aerosol size distribution and the ability of atmospheric aerosol particles acting as CCN (CCN activity) (Fitzgerald, 1973). Thus, field measurements of aerosol size distribution and physicochemical properties are needed to better understand the radiative forcing exerted by atmospheric aerosol particles.

Previous studies suggest that particle number size distribution (PNSD) is a primary factor influencing CCN concentrations (Dusek et al., 2006; Rose et al., 2010; Pöhlker et al., 2016; Burkart et al., 2011). The PNSD can account for 84–96% of the variability in the CCN concentrations (N_{CCN}) (Dusek et al., 2006), while CCN activities may also play a significant role in the N_{CCN} (Quinn et al., 2008; Cai et al., 2018; Ovadnevaite et al., 2017; Liu et al., 2018; Crosbie et al., 2015), which are primarily governed by the particle size, chemical composition, mixing state, surface tension, and hygroscopicity (Köhler, 1936; Seinfeld and Pandis, 2016). Among these factors, the impact of hygroscopicity on CCN activities has received great attention in recent years (Petters and Kreidenweis, 2007; Ajith et al., 2022; Rose et al., 2010). Petters and Kreidenweis (2007) proposed the κ- Köhler theory based on the Köhler theory to quantify the ability of aerosol particles to absorb moisture and become CCN based on the aerosol hygroscopicity parameters (κ). Ajith et al. (2022) showed that 64% of particles can be activated as CCN when κ is equal to 0.37, whereas when κ decreases to 0.23, only 48% of particles can be activated in the tropical coastal area.

Significant seasonal variations in PNSD and hygroscopicity under both terrestrial and marine environments were observed in previous field observations, leading to the seasonal variations in N_{CCN} (Crosbie et al., 2015; Schmale et al., 2018; Burkart et al., 2011; Bougiatioti et al., 2009; Sihto et al., 2011; Leena et al., 2016; Ross et al., 2003; Gras and Keywood, 2017; Quinn et al., 2019). Crosbie et al. (2015) revealed that in the urban area of Arizona particles had larger sizes, higher hygroscopicity, and N_{CCN} was also higher during winter, while a higher abundance of smaller particles was observed during summer owing to stronger photochemical reactions. In pristine environments like mountain, coastal, and forested

regions, seasonal variations in N_{CCN} and PNSD were more pronounced than urban and rural areas (Schmale et al., 2018). Pöhlker et al. (2016) observed significant differences in N_{CCN} between the wet and dry seasons in the Amazon rainforest, while the κ values remained relatively stable. They also noted increased particle concentrations and aerosol hygroscopicity, both subject to the impact of long-range transport originating from anthropogenic emissions. Observations in marine areas during different seasons are relatively scarce compared with those in inland areas. Gras (1995) found that both particle concentration and N_{CCN} in the Southern Ocean reached their peaks during summer and gradually decrease to their valleys in winter. Quinn et al. (2019) showed that sea spray aerosols make a relatively significant contribution to N_{CCN} only during winter in the Western North Atlantic, while in other seasons, the primary contribution comes from biogenic aerosols oxidized from dimethyl sulfide (DMS). Zheng et al. (2020) revealed that sulfate dominates the particle condensational growth to CCN sizes during summer in the North Atlantic, while secondary organic aerosols played a significant role in particle growth throughout all seasons. These results indicate that CCN activity and concentration could vary in a large range during different seasons. Thus, further observations across different seasons in marine environments are needed to enhance our understanding of marine CCN activities and their seasonal variations.

The South China Sea (SCS), located in Southeast Asia and bordered by China, the Indochinese Peninsula, and Maritime Southeast Asia, is significantly influenced by air pollutants transported through terrestrial air masses. Studies have shown that these pollutants play a crucial role in determining aerosol concentration and properties in the region (Atwood et al., 2017; Xiao et al., 2017; Geng et al., 2019; Liang et al., 2021; Sun et al., 2023; Qin et al., 2024). For instance, Xiao et al. (2017) reported that 69.7% of nitrate and 57.5% of sulfate in the SCS originated from fossil fuel combustion, particularly coal burning in Chinese coastal regions. Additionally, Liang et al. (2021) and Sun et al. (2023) observed an increase in the organic fraction and concentration of submicron aerosols when the region was influenced by terrestrial air masses from Mainland China and the Indochinese Peninsula in the northern SCS. Further studies highlighted the variation in aerosol properties under different air mass influences. Atwood et al. (2017) found a significant bimodal particle distribution with a κ value of 0.65 in the southern SCS under marine air mass influence, whereas a unimodal distribution with a κ of 0.4 was observed under continental air mass influence.

The SCS experiences a typical monsoon climate with distinct seasonal wind direction changes (Wang et al., 2009). The northeast monsoon, occurring from November to March, is characterized by

stronger average wind speeds and longer period compared to the southwest monsoon, which dominates from June to August. The transitional periods occur from April to May and September to October. During the northeast monsoon, air pollutants are primarily transported to the SCS by terrestrial air masses from China (Xiao et al., 2017; Liu et al., 2014; Geng et al., 2019). In contrast, during the summer, pollutants mainly originate from terrestrial air masses from the Indochinese Peninsula and Maritime Southeast Asia (Geng et al., 2019; Liang et al., 2021; Sun et al., 2023). These varying sources of anthropogenic emissions exerts different impacts on CCN activity differently across seasons. Additionally, the fraction of high cloud over the SCS varies from approximately 0.3 to 0.7 across different months, indicating that aerosol-cloud interactions in the region may differ between seasons (Lu et al., 2022). However, due to limited observational data, our understanding of seasonal variations in CCN activity in the SCS remains incomplete. Conducting comprehensive observational studies on CCN activity across different seasons is essential for improving our understanding of aerosol-cloud interactions on the SCS.

In this study, we conducted two shipborne observations in the SCS during summer (May 5–June 9, 2021) and winter (December 19–29, 2021). Our observations with online instruments focused on measuring aerosol chemical composition, PNSD, and CCN activation in the region. Our results provide valuable insights into the differences in CCN activity between winter and summer, as well as the influence of different types of terrestrial air masses on CCN activity in the SCS across different seasons.

2. Methodology

2.1 Cruise information and onboard measurements

2.1.1 Cruise information

This study consists of two research cruises conducted during the summer and winter of 2021, respectively. These two cruises were interdisciplinary scientific expeditions, integrating fields such as marine geology, oceanography, and atmospheric environment. The primary objective in atmospheric environment was to investigate the impact of summer and winter monsoons on the atmospheric environment of the South China Sea (SCS). The summer and winter cruises were carried out respectively by the vessels "Tan Kah Kee" and "Sun Yat-sen University". The "Tan Kah Kee" is an oceanographic research vessel with a length of 77.7 meters, a beam of 16.24 meters, and a displacement of 3611 tons. The "Sun Yat-sen University" is a comprehensive oceanographic training vessel with a total length of 114.3 meters, a beam of 19.4 meters, and a displacement of 6880 tons.

The first cruise was from May 5th to June 9th, 2021. The cruise started from Xiamen Port and traversed from the northern to the central-southern South China Sea, and then circled back near Hainan Island, and finally returned to Xiamen Port. The second cruise was from December 19th to December 29th, 2021. It began from Gaolan Port in Zhuhai and reached the vicinity of Yongxing Island, and ultimately returned to Gaolan Port (Fig. 1a). Unfortunately, due to adverse weather conditions, such as strong winter monsoon winds causing poor sea conditions, and the fact that it was the first scientific deployment of the research vessel Sun Yat-sen University, the winter cruise had a shorter duration and covered a narrower spatial range, remaining only in the northern SCS (Fig. S1), compared to the summer cruise. On both cruises, most of the instruments were housed in a single compartment and the sampling lines were extended from the window of the compartment to the height of the ship's bridge (~17 m above sea level) (Fig. 1a).

2.1.2 Size-resolved cloud condensation nuclei activity measurement

The size-resolved CCN activity was measured with a combination of a scanning mobility particle sizer (SMPS) system and a cloud condensation nuclei counter (model CCNc-200, DMT Inc., USA), the scanning mobility CCN analysis (SMCA) method initially proposed in Moore et al. (2010). The SMPS system consisted of a differential mobility analyzer (DMA; model 3082, TSI., Inc.) and a condensation particle counter (CPC; model 3756, TSI Inc.). The SMPS and the CCNc system were used to measure PNSD and size-resolved CCN number concentration at a mobility size range of 10–500 nm and 10–593 nm in summer and winter campaign, respectively. Unfortunately, due to the malfunction of flow sensor in the column B, only the data from column A is presented in this study. During the SMCA measurement, the particles were first passed through a Nafion dryer to remove moisture, then neutralized using a neutralizer. After that, they were subjected to size selection with a DMA. The particles were then split between a CPC (1 L min^{-1}) for particle concentration measurement and a CCNc (0.5 L min^{-1}) for CCN measurement at a specific supersaturation. To maintain sample flow through the DMA, dilution air (0.5 L min^{-1}) was added to the CPC inlet stream. The effect of the dilution air was accounted for in the PNSD data processing (Fig. S2). The supersaturation (SS) of the CCNc was set at 0.2 %, 0.4 %, and 0.7 % in summer campaign and 0.1%, 0.2 %, 0.4 %, and 0.7 % in winter campaign, respectively. Before the measurements, the CCNc was calibrated with ammonium sulfate ($(NH_4)_2SO_4$) particles at each set SS. Detailed description of the instrument configuration and calibration can be found in Cai et al. (2018).

2.1.3 Aerosol chemical composition measurement

The chemical composition of atmospheric non-refractory submicron particulate matter (NR-PM_1), including sulfate, nitrate, organics, ammonium, and chloride, was measured using an online time-of-flight ACSM (ToF-ACSM; Aerodyne Inc., USA). The sampling time of the ToF-ACSM was approximately 10 min. The relative ionization efficiency (RIE) values of the instrument were calibrated using ammonium nitrate (NH_4NO_3) and ammonium sulfate ($(NH_4)_2SO_4$) both before the start and after the completion of the campaigns. The RIE values for ammonium were 3.31 and 3.33 during the summer and winter, respectively, while the ones for sulfate were 1.02 and 0.81 during the summer and winter, respectively. The collection efficiency (CE) was determined as shown in Sun et al. (2023) and time-independent CE values were used in this study. Detailed CE calculation can be found in the supplementary (Text S1, and Fig. S3). The black carbon concentrations were measured with an aethalometer (AE33, Magee Scientific).

2.1.4 Meteorological parameter measurements

The meteorological elements, including temperature, relative humility, wind speed, and wind direction, were measured by the combined automatic weather station onboard the vessels. During the winter cruises, meteorology data before 12.22 was missed due to the calibration for the automatic weather station before 12.22. The timeseries of meteorological data were presented in Fig. S4.

2.2 Data analysis

2.2.1 CCN activation

The size-resolved number concentration of total particle and cloud condensation nuclei were obtained from the SMPS and CCNc thourgh the SMCA method. The activation diameter was determined by fitting the activation ratio (AR, N_{CCN}/N_{CN}) and dry diameter at each supersaturation through the following equation:

$$AR = \frac{B}{1+\left(\frac{D_P}{D_{50}}\right)^C}, \quad (1)$$

where AR indicates the size-resolved AR, D_P represents dry particle diameter (nm); B, C, and D_{50} are the three fitting parameters, representing the asymptote, the slope, and the inflection point of the sigmoid, respectively (Moore et al., 2010). The D_{50} parameter, also known as the critical diameter, corresponds to

196 the particle size at which 50% of the particles are activated at a specific SS. The fitting results from
197 SMCA method measured in this study are presented in Fig. S5.

198 The hygroscopicity parameter (κ) which represents CCN activity according to κ-Köhler equation is
199 calculated as follows (Petters and Kreidenweis, 2007):

200 $$\kappa = \frac{4A^3}{27{D_{50}}^3(lnS_c)^2},\ A = \frac{4\sigma_{s/a}M_w}{RT\rho_w} \quad (2)$$

201 where ρ_w is the density of pure water (about 997.04 kg m^{-3} at 298.15 K), M_W is the molecular weight of
202 water (0.018 kg mol^{-1}), $\sigma_{s/a}$ corresponds to the surface tension of the solution-air interface and is assumed
203 to be equal to the surface tension of pure water ($\sigma_{s/a}$=0.0728 N m^{-1} at 298.15 K), R is the universal gas
204 constant (8.314 J mol^{-1} K^{-1}), T denotes thermodynamic temperature in kelvin (298.15 K), and D_{50} is the
205 critical diameter (in m). Additionally, it is noting that the estimated κ values refer to particles with the
206 D_{50}, which are the smallest particles that can be activated at a given SS.

207 During part of the summer measurement period, the D_{50} at 0.7% supersaturation ranged between 30
208 and 40. However, due to lower concentrations during these times, instrument noise introduced greater
209 measurement uncertainty, as demonstrated in Fig. S6. Consequently, the average D_{50} and κ at 0.7% SS
210 are not included in Table 1.

211 **2.2.2 Closure Method**

212 According to Petters and Kreidenweis. (2007), κ can be predicted by a simple mixing rule based
213 on chemical volume fractions:

214 $$\kappa_{sim} = \sum_i \varepsilon_i \kappa_i \quad (3)$$

215 where ε_i and κ_i are the volume fraction and hygroscopicity parameter for the specific dry
216 component in the mixture. We obtained ε from aerosol chemical composition measured by the ToF-
217 ACSM. In this study, κ for $(NH_4)_2SO_4$ (0.48), NH_4NO_3 (0.58), and NaCl (1.1) represent the κ of SO_4^{2-},
218 NO_3^-, and Cl^- provided by the ToF-ACSM (Huang et al., 2022). Besides, the κ of organic was 0.1 at this
219 study according to Huang et al. (2022). The density of $(NH_4)_2SO_4$, NH_4NO_3, NaCl and organic are 1769
220 kg m^{-3}, 1720 kg m^{-3},2165 kg m^{-3}, and 1400 kg m^{-3} (Huang et al., 2022; Gysel et al., 2007).

2.2.3 CCN concentration and activation ratio calculation

Due to the malfunction of the column B, the CCN concentration (N_{CCN}) was calculated based on the size-resolved AR at a specific SS from SMCA method and observed particle number concentration. It can be calculated by the following equation (Cai et al., 2018):

$$N_{CCN}(SS) = \int_0^{\infty} AR(SS, D_P) N_{CN}(D_P) dD_p \quad (4)$$

where N_{CCN} (SS) is the CCN concentration at a specific SS, AR(SS, D_p) is the ratio of N_{CCN} at a specific SS to N_{CN} on a specific diameter from the SMCA method and $N_{CN}(D_P)$ is the particle number concentration at a specific diameter (Dp). Due to the absence of direct measurements for total N_{CCN}, we refer to the N_{CCN} derived from Eq. (4) as observed values ($N_{CCN,obs}$) in this study. Previous research has shown that this method (size-resolved CCN from one column in CCNc-200) provides results closely matching those obtained from direct measurement (from another column in CCNc-200), supporting its reliability (Meng et al., 2014; Lathem and Nenes, 2011).

The N_{CCN} (referred as $N_{CCN,sim}(SS)$) can be predicted by D_{50} from closure method ($D_{50,sim}(SS)$) and N_{CN} according to following equation (Jurányi et al., 2011):

$$N_{CCN,sim}(SS) = \int_{D_{50,sim}(SS)}^{\infty} N_{CN}(D_P) dD_p \quad (5)$$

where the $D_{50,sim}(SS)$ is calculated based on the eq. (2) and (3).

The bulk AR at a specific SS can be calculated by:

$$AR(SS) = \frac{N_{CCN,obs}(SS)}{N_{CN,tot}} \quad (6)$$

where the $N_{CN,tot}$ represents the total particle number concentration.

To investigate the impact of the fraction and mixing state of aerosol on N_{CCN}, two CCN simulation scheme are applied in this study (Patel et al., 2021).

(1) Internal-mixed scheme: the aerosol composition from the ToF-ACSM was assumed to be size-independent and internally mixed. All aerosol has an identical chemical composition in the whole size range. N_{CCN} is calculated by K_{sim} and measured PNSD according to Eq. (2), Eq. (3), and Eq. (5) (Fig. S7a).

(2) External-mixed scheme: the aerosol composition from the ToF-ACSM was assumed to be size-independent and externally mixed. Four type of aerosol ($(NH_4)_2SO_4$, NH_4NO_3, NaCl and organic) are assumed to have a same proportion for all sizes. The D_{50} from each species was

calculated according to their κ values mentioned in 2.2.2. N_{CCN} is calculated according to the Eq. (5) (Fig. S7b).

To access the simulation result from these two schemes, normalized mean bias (NMB) was used in this study:

$$NMB = \frac{\sum(N_{CCN,sim} - N_{CCN,obs})}{\sum N_{CCN,obs}} \quad (6)$$

where $N_{CCN,sim}$ is the simulated N_{CCN} from two schemes, and $N_{CCN,obs}$ is the observed N_{CCN}.

2.2.4 Backward trajectory simulation and cluster analysis

Backward trajectory calculations were performed using the MeteoInfo, an open-source software (Wang, 2014) to determine potential source origins. Weekly GDAS1 (Global Data Assimilation System at a resolution of 1°) files were downloaded from the NOAA Air Resource Laboratory (ARL) website (https://www.ready.noaa.gov/gdas1.php). The calculation of backward trajectories is performed every 1hour based on the location mentioned below, generating 72-hour backward trajectories at 500m.

To clarify the sources of air masses, the cluster analysis was applied in this study, which was performed by TrajStat, a plug-in module of MeteoInfo, based on k-means method (http://meteothink.org/docs/trajstat/cluster_cal.html). According to the report by the China Meteorological Administration (Chao et al., 2022), the summer monsoon in 2021 broke out during the sixth pentad of May. Therefore, based on the timing of the monsoon onset and the actual trajectory of the ship, we selected two representative midpoints of the ship track for backward trajectory calculations and cluster analysis in summer: the midpoint of the ship's track before the onset of the summer monsoon (May 5-23) and the midpoint of the track after the summer monsoon began (May 24-June 9). In the winter cruise, backward trajectories calculation and cluster analysis was performed at two specific locations: the ship's anchorage near Big Ten-thousand Mountain Island (December 19-22 and December 27-29) and the midpoint between Dawan Mountain Island and Yongxing Island (December 23-26). To ensure the accuracy of the backward trajectory calculations and cluster analysis, we compared the trajectories at the midpoints with those from the ship's actual locations to verify consistency in air mass sources (Fig. S8). We further examined the trajectories for each cluster to verify their alignment with the air mass origins they represent (Fig. S9). The results demonstrate that cluster analysis was well-conducted. Additionally, figure S10 illustrates the average altitude variation as the age in hours increases across different periods. During summer, the altitude of the clusters remained below 880 hPa, indicating

that they resided within the boundary layer (about 800 hPa). While in winter, the altitude of the clusters was higher than in summer, especially for the cluster during the mixed period (peaked at about 755 hPa). However, these clusters were generally within or close to the boundary layer. These results suggest that the back trajectories could represent the characteristics of the air masses originating from these specified regions.

2.2.5 Data quality control

To ensure reliable atmospheric samples in the SCS and mitigate the influence of research vessel emissions, we applied the following data processing procedures (Huang et al., 2018; Cai et al., 2020; Liang et al., 2021).

Firstly, we identified organic compounds, black carbon (BC), and small particulate matter (41.4 nm particles) as indicators of ship emissions, recognizing their sudden peak values as indicative of the ship's own emissions.

Secondly, we accounted for the relative positions of the ship's chimney and the sampling tube. During the summer cruise, we excluded data corresponding to a relative wind direction (with respect to the ship's bow) between 150° and 270° and a relative wind speed (with respect to the ship's speed) of less than 2.5 m s^{-1} (Fig. S11a, Fig. S12a1, and Fig. S13a-c). During the winter cruise, we excluded data for a relative wind direction between 150° and 220° and a relative wind speed of less than 2.5 m s^{-1} (Fig. S11b, Fig. S12b1, and Figs. S13d-f).

Applying these criteria, 74.8% of the data in summer and 92.2% in winter (both at 10-minute resolution) were classified as “clean” and retained for analysis. The timeseries of data before and after quality control is shown in Fig. S14.

3. Results and discussion

3.1 CCN concentration and aerosol characteristics over SCS in summer and winter

Figure 2 presented the timeseries of PNSD (a1 and a2), NR-PM_1 mass concentrations and fractions (b1 and b2, c1 and c2), number concentrations of CCN (d1 and d2), and hygroscopicity κ-values (e1 and e2) during two campaigns in summer and winter. During the summer cruise, we observed two distinct periods around the onset of the summer monsoon. The South China Sea (SCS) summer monsoon began in the sixth pentad of May (Chao et al., 2022). In winter, the influence of the winter monsoon persisted

306 throughout the entire observation period (Fig. 1c). Despite our measurements being limited to the
307 northern SCS in winter, the impact of the Northeast Monsoon on the SCS was evident.

308 The average particle number concentration in summer (6966 cm^{-3}) was higher than in winter (4988
309 cm^{-3}), primarily due to the higher number concentration of Aitken-mode particles in summer (Fig. 3a-b).
310 In summer, particles were concentrated in smaller sizes, whereas in winter, particle size distribution was
311 relatively balanced between the Aitken mode (2185 cm^{-3}) and the accumulation mode (2176 cm^{-3}) (Fig.
312 3a-b).

313 The average mass concentration of NR-PM_1 was 3.76 μg m^{-3} in summer and increased to 9.39 μg
314 m^{-3} in winter (Fig. 3c-d). In summer, the dominant aerosol component was sulfate (45.5%), followed by
315 organics (35.8%), ammonium (12.9%), nitrate (4.0%), and chloride (1.9%) (Fig. 3c), similar to the
316 pattern observed in the northern SCS during the summer of 2018 (Fig. 3e) (Liang et al., 2021). However,
317 in winter, organics became the predominant aerosol component (37%), with nitrate (22.2%) replacing
318 sulfate (18.9%) as the highest proportion of inorganic components (Fig. 3d). Although N_{CN} were higher
319 in summer than in winter, the particle volume size distribution indicates that a higher fraction of particles
320 was concentrated in larger size in winter, which significantly influenced mass concentration, resulting in
321 a higher NR-PM_1 concentration (Fig. S15).

322 The average number concentration of cloud condensation nuclei (N_{CCN}) in summer was higher than
323 in winter at all supersaturation (SS) levels (Table 1). The ratio of N_{CCN} between summer and winter was
324 smaller at high SS ($N_{CCN,\,winter}/N_{CCN,summer}$ = 0.51 and 0.54 at 0.4% SS and 0.7% SS, respectively)
325 compared to low SS ($N_{CCN,\,winter}/N_{CCN,summer}$ = 0.62 at 0.2% SS), likely due to the significant difference in
326 number concentration of Aitken-mode particles between the two seasons (Fig. 3a-b). Compared to the
327 observation in the Yellow Sea, a region similarly influenced by terrestrial air masses from mainland
328 China, the N_{CCN} were lower in winter, while in summer, the N_{CCN} were more comparable to those
329 observed in the Yellow Sea (4821 cm^{-3} at 0.63% SS) (Park et al., 2018).

330 The aerosol hygroscopicity (κ) was higher in summer than that in winter (Table 1). Besides, the
331 hygroscopicity pattern varied between seasons: in summer, κ increased with SS (from 0.47 to 0.54
332 between 0.2% SS and 0.4% SS), while in winter, κ decreased with SS (from 0.50 to 0.15 between 0.1%
333 SS and 0.7% SS) (Fig. 3a-b). The winter κ pattern was similar to observations in the Western North
334 Pacific (Table 1) (Kawana et al., 2020). Additionally, the winter κ values were comparable to those in

Guangzhou (Cai et al., 2020), adjacent to the SCS, indicating that the northern SCS is influenced by air masses from Mainland China under the significant influence of the Northeast Monsoon during winter.

3.2 Anthropogenic influence on CCN concentration in different season

Cluster analysis revealed distinct periods influenced by various air masses. In summer, three terrestrial air mass sources were identified: Luzon Island (referred to as "Luzon"), Palawan Island, and the Indochinese Peninsula, along with a marine air mass source (Fig. 4a). Given the limited influence of air masses from Palawan Island, this period was excluded from the study. Consequently, the study focused on periods dominated by air masses from Luzon ("Luzon" period), the Indochinese Peninsula ("Indochinese Peninsula" period), and marine sources ("Marine-s" period). In winter, the air mass sources included Mainland China, a mixture of Mainland China and the South China Sea (referred to as "Mixed"), and a marine source (Fig. 4b). These were classified as the "Mainland China" period, "Mixed" period, and "Marine-w" period, respectively.

As shown in figure 5, terrestrial air masses could significantly affect the aerosol chemical composition in the SCS, resulting in higher NR-PM_1 mass concentration and a higher fraction of organic compounds compared to those influenced by marine air masses. Additionally, the particles number concentration in the accumulation mode and the N_{CCN} at low supersaturation (SS) were higher during periods influenced by terrestrial air masses ("Luzon" period) than those during marine air mass periods (Table 2). Notably, we were able to obtain an accurate D_{50} at 0.7% supersaturation only during the "Luzon" period in summer. Due to the relatively lower hygroscopicity compared to other summer periods, the corresponding D_{50} at 0.7% SS ranged between 40 and 60 nm, with relatively high concentration of CN and CCN (Fig. S6), allowing for a more precise measurement of D_{50}. As a result, the κ at 0.7% SS shown in Fig. 7 was specific to the Luzon period in summer.

In summer, the "Luzon" period exhibited the highest N_{CN}, attributed to the elevated particle concentration in the Aitken mode, compared to all other periods in both summer and winter (Fig. 6a and Table 1). This high fraction of Aitken mode particles leaded to the lowest bulk AR among the summer periods (Fig. 7a), as a larger fraction of particles centered on a size range lower than the D_{50} (Fig. 7b). Furthermore, the prevalence of a higher fraction of Aitken mode particles during terrestrial air mass periods is commonly correlated with the influence of fresh anthropogenic emissions (Beddows et al., 2015), which could lower the hygroscopicity and consequently suppress the bulk AR.

In the “Indochinese Peninsula” period, the N_{CN} was lower than it in the “Marine-s” period (Table 2). This difference was mainly due to the variation of Aitken mode particles, while accumulation mode particles were higher during the “Indochinese Peninsula” period than in “Marine-s” period (Table 2). The “Marine-s” period primarily occurred during the transition phase before the onset of summer monsoon, when wind direction shifted from east (Luzon Island direction) to southwest (Indochinese Peninsula direction). Anthropogenic emissions from Luzon Island still affected the marine atmosphere, leading to higher concentrations of Aitken mode particles compared to the “Indochinese Peninsula” period (Table 2). The higher fraction of accumulation mode particles and higher hygroscopicity during the “Indochinese Peninsula” period resulted in a higher bulk AR compared to the “Luzon” period. Despite a higher organic fraction in NR-PM_1 during the “Indochinese Peninsula” period (Fig. 5), hygroscopicity was still higher due to a higher oxidation degree of organics, indicated by a higher m/z 44 to 43 ratio (5.87 compared to 5.60 in the “Luzon” period) (Lambe et al., 2011; Jimenez et al., 2009). Additionally, higher wind speeds during this period (7.26 m s^{-1} compared to 3.18 m s^{-1} in the “Luzon” period) leaded a higher fraction of sea salt (Huang et al., 2022), resulting a higher aerosol hygroscopicity. Unfortunately, owing to instrument limit, sea salt cannot be detected by the ToF-ACSM.

In winter, nitrate accounted for the highest fraction of NR-PM_1 (25.4%) during the “Mainland China” period compared to other periods (Fig. 5d). Due to similar hygroscopicity between nitrate and sulfate, as well as comparable inorganic fractions between the “Mainland China” and “Luzon” periods, κ at 0.2% SS was also similar between these two periods (0.30 and 0.33, respectively) (Fig. 7b). However, aerosol hygroscopicity at small sizes was much lower in the “Mainland China” period than in the “Luzon” period (Fig. 7b), contributing to the low bulk AR in the “Mainland China” period (Fig. 7a). The BC mass concentration was higher during the “Mainland China” period (2.25 μg m^{-3}) compared to the “Luzon” period (0.72 μg m^{-3}). This suggests that the lower hygroscopicity in smaller particles during the “Mainland China” period may be attributed to a larger fraction of hydrophobic BC. Additionally, hygroscopicity at smaller sizes was consistently lower across all winter periods, including the “Mainland China” period, compared to summer. This phenomenon may be related to the reduced sulfate fraction in smaller sizes during winter, as sulfate production via DMS oxidation is diminished due to lower sea surface temperatures in winter (18.0°C) compared to summer (29.3°C), which in turn inhibits DMS production by phytoplankton (Bates et al., 1987). The similar fractions of Aitken mode and accumulation

particles indicated that PNSD could not fully explain the low bulk AR in the "Mainland China" period. Overall, lower N_{CN} and bulk AR in the "Mainland China" period compared to the "Luzon" period resulted in a lower N_{CCN}.

During the "Mixed" period, N_{CCN} was lower than in the "Mainland China" period, which can be attributed to the decreased N_{CN} (Table 2). However, accumulation mode particles dominated, unlike in other terrestrial air mass periods (Fig. 6), resulting in a significantly higher bulk AR compared to the "Mainland China" period. Organic aerosol hygroscopicity was also higher during the "Mixed" period, supported by a higher m/z 44 to 43 ratio (3.88 vs. 3.10 in the "Mainland China" period), which explains the greater hygroscopicity despite a higher organic fraction in NR-PM_1. Additionally, the lower BC concentration in the "Mixed" period (1.20 μg m^{-3} vs. 2.25 μg m^{-3} in the "Mainland China" period) suggests a smaller BC fraction. Moreover, the higher wind speeds during the "Mixed" period (10.77 m s^{-1} vs. 7.14 m s^{-1} in the "Mainland China" period) could have increased the sea salt fraction, further enhancing aerosol hygroscopicity..

3.3 CCN closure analysis

The CCN closure study is widely used to assess the impact of various factors on CCN activity (Patel et al., 2021; Cai et al., 2018; Meng et al., 2014; Deng et al., 2013). In this study, we applied two schemes based on the CCN closure method, as described in Section 2.2.3, which consider aerosol composition and mixing state. The fitting parameters and coefficient of determination (R^2) are presented in Table 3, while the fitting plots for both schemes are shown in Figures S16 and S17. Besides, the NMB from these schemes was presented in Fig. 8.

In summer, the NMB was always lower than 0, which indicated that simulated aerosol hygroscopicity was lower than observed value (Fig. 8). Sea salt which cannot be detected by the ToF-ACSM may account for higher fraction in summer due to low aerosol concentration in summer (Fig. 3c), resulting in the underestimation of aerosol hygroscopicity. The NMB exhibits similar trends with changes in SS in all three periods in summer. Better fitting result appeared at high SS, which indicated a greater underestimation of the hygroscopicity of larger particles. Besides, "Internal-mixed" scheme had more precious result than it in "External-mixed" scheme in summer (Fig. 8), suggesting the aerosol was primary internally mixed in summer.

In winter, the "External-mixed" scheme always showed a better result than "Internal-mixed" scheme at high SS (0.4% SS and 0.7% SS), indicating that particles in small size were mainly externally mixed. Considering the low hygroscopicity of small-sized particles in winter, it is likely that a significant fraction of these particles consists of externally mixed BC, which probably originated from fresh anthropogenic emissions and remains unmixed with other inorganic salts and organics. As BC ages, inorganic and organic components adhere to it, which would lead to the increase of diameter and particles tended to be internally mixed (Sarangi et al., 2019). This transition resulted in higher hygroscopicity in large-sized particle compared to the smaller-sized particles. Besides, overestimation of aerosol hygroscopicity at high SS could be owing to a higher fraction of non- or less- hygroscopic component (such as organic and BC) at small particle sizes. The predicted N_{CCN} at 0.1% SS are 20%-40% lower than the observed concentrations, whereas the predictions at 0.2% SS more closely match the observed values (Fig. 8). This discrepancy may be due to the higher fraction of sea salt in larger particles. However, due to instrumental limitations, the ToF-ACSM cannot detect BC and sea salt. Future observations including BC and sea salt are needed to better assess their effects on aerosol hygroscopicity in the South China Sea (SCS). In addition, further study of size-resolved aerosol composition can also enhance the understanding on CCN activity in the SCS.

4. Conclusion

In this study, we investigated the seasonal variations of cloud condensation nuclei (CCN) activity in the South China Sea (SCS) and explored the impact of anthropogenic emissions. Shipborne observations were conducted during the summer (May 5–June 9) and winter (December 19–29) of 2021. We measured CCN activity, chemical composition, and particle number size distribution (PNSD) using several onboard instruments, including a ToF-ACSM, a CCNc, an SMPS, and an AE33. Observations included periods before and after the summer monsoon onset and periods influenced by the winter monsoon.

Our results show that particle number concentration (N_{CN}) and CCN number concentration (N_{CCN}) were higher in summer than in winter, while the mass concentration of non-refractory submicron particulate matter (NR-PM_1) was lower in summer. This difference is primarily attributed to the predominance of Aitken mode particles in summer, contrasted with a higher concentration of

accumulation mode particles in winter. Additionally, aerosol hygroscopicity and bulk AR were found to be higher in summer than in winter.

Backward trajectory and cluster analyses identified distinct influences from various air masses. In summer, we identified periods affected by terrestrial air masses from Luzon Island (the “Luzon” period) and the Indochinese Peninsula (the “Indochinese Peninsula” period), alongside a period influenced by marine air masses (the “Marine-s” period). In winter, the periods were influenced by terrestrial air masses from Mainland China (the “Mainland China” period), a mix of Mainland China and marine sources (the “Mixed” period), and marine air masses (the “Marine-w” period). Terrestrial air mass periods exhibited higher NR-PM_1 mass concentrations, organic fractions, and N_{CCN}, particularly at low supersaturation, compared to those influenced by marine air masses.

During the “Luzon” period, high N_{CCN} was observed, attributed to high N_{CN}, especially in the Aitken mode. This high concentration in the Aitken mode resulted in a low bulk AR at 0.2% SS, indicating a higher fraction of primary organic aerosol with low hygroscopicity. This caused lower overall hygroscopicity compared to other summer periods. The lower ratio of m/z 44 to 43 also suggested a lower oxidation degree of organics in this period. In the "Indochinese Peninsula" period, higher fraction of the accumulation mode particles comparted to the "Luzon" period led to a higher bulk AR, combined with increased hygroscopicity.

In winter, the "Mainland China" period was characterized by a high nitrate fraction in the NR-PM_1. The similar inorganic fractions in the NR-PM_1 between the “Mainland China” and “Luzon” periods resulted in comparable aerosol hygroscopicity at low supersaturation (0.2% SS). However, at higher supersaturation levels (0.4% and 0.7% SS), the “Mainland China” period demonstrated significantly lower hygroscopicity, which led to a reduced bulk AR at elevated supersaturation. During the "Mixed" period, accumulation mode particles predominated, leading to a high bulk AR. This indicated an aging process during transport, with more oxidized organics and higher aerosol hygroscopicity. The lower black carbon (BC) fraction and the higher sea salt fraction from high wind speed contributed to higher hygroscopicity in the "Mixed" period compared to the "Mainland China" period, despite the high organic fraction.

The CCN closure analysis, considering aerosol composition and mixing state, revealed that aerosols in summer were primarily internally mixed, while in winter, small-sized aerosols were primarily externally mixed. This distinction is crucial for climate models predicting N_{CCN} in the SCS. The

underestimation of aerosol hygroscopicity in summer suggests that the effect of sea salt should be considered.

Our study highlights significant seasonal differences in CCN activity in the SCS and the influence of different types of terrestrial air masses. Future measurements including size-resolved aerosol composition and obtain more precise measurements of BC and sea salt are needed to better understanding CCN activity in this region. Additionally, our observation in winter focused on the CCN activity over the northern SCS, while the influence of air masses from Mainland China in remote SCS was still unclear. Further observations in remote SCS areas could help clarify the anthropogenic influence during winter under the effect of the winter monsoon.

Data availability. Data from the measurements are available at https://doi.org/10.6084/m9.figshare.25472545 (Ou et al., 2024).

Supplement. The supplement related to this article is available online at xxx.

Author contributions. **HO, MC, and JZ** designed the research. **YZ**, **XN, BL, and CS** performed the measurements. **HO, MC, QS, and SM** analyzed the data. **SZ and HW** provided useful comment on the paper. **HO, MC,** and **JZ** wrote the paper with contributions from all co-authors.

Competing interests. The authors declare that they have no conflict of interest.

Financial support. This work was supported by National Natural Science Foundation of China (NSFC) (Grant No. 42305123 and 42175115) and Basic and Guangzhou Applied Basic Research Foundation (Grant No. 2023A1515012240 and 2024A1515030221).

Acknowledgements. Additional support from the crew of the vessels "Tan Kah Kee" and "Sun Yat-sen University" is greatly acknowledged.

Reference

Ajith T. C, Kompalli, S. K., and Babu, S. S.: Role of Aerosol Physicochemical Properties on Aerosol Hygroscopicity and Cloud Condensation Nuclei Activity in a Tropical Coastal Atmosphere, ACS Earth Space Chem, 6, 1527-1542, doi:https://doi.org/10.1021/acsearthspacechem.2c00044, 2022.

Albrecht, B. A.: Aerosols, cloud microphysics, and fractional cloudiness, Science, 245, 1227-1230, doi:https://doi.org/10.1126/science.245.4923.1227, 1989.

Atwood, S. A., Reid, J. S., Kreidenweis, S. M., Blake, D. R., Jonsson, H. H., Lagrosas, N. D., Xian, P., Reid, E. A., Sessions, W. R., and Simpas, J. B.: Size-resolved aerosol and cloud condensation nuclei (CCN) properties in the remote marine South China Sea - Part 1: Observations and source classification, Atmos. Chem. Phys., 17, 1105-1123, doi:https://doi.org/10.5194/acp-17-1105-2017, 2017.

Bates, T. S., Cline, J. D., Gammon, R. H., and Kelly-Hansen, S. R.: Regional and seasonal variations in the flux of oceanic dimethylsulfide to the atmosphere, J. Geophys. Res. Oceans, 92, 2930-2938, doi:https://doi.org/10.1029/JC092iC03p02930, 1987.

Beddows, D. C. S., Harrison, R. M., Green, D. C., and Fuller, G. W.: Receptor modelling of both particle composition and size distribution from a background site in London, UK, Atmos. Chem. Phys., 15, 10107-10125, doi:https://doi.org/10.5194/acp-15-10107-2015, 2015.

Bougiatioti, A., Fountoukis, C., Kalivitis, N., Pandis, S. N., Nenes, A., and Mihalopoulos, N.: Cloud condensation nuclei measurements in the marine boundary layer of the eastern Mediterranean: CCN closure and droplet growth kinetics, Atmos. Chem. Phys., 9, 7053-7066, doi:https://doi.org/10.5194/acp-9-7053-2009, 2009.

Burkart, J., Steiner, G., Reischl, G., and Hitzenberger, R.: Long-term study of cloud condensation nuclei (CCN) activation of the atmospheric aerosol in Vienna, Atmos Environ, 45, 5751-5759, doi:https://doi.org/10.1016/j.atmosenv.2011.07.022, 2011.

Cai, M. F., Liang, B. L., Sun, Q. B., Zhou, S. Z., Chen, X. Y., Yuan, B., Shao, M., Tan, H. B., and Zhao, J.: Effects of continental emissions on cloud condensation nuclei (CCN) activity in the northern South China Sea during summertime 2018, Atmos. Chem. Phys., 20, 9153-9167, doi:https://doi.org/10.5194/acp-20-9153-2020, 2020.

Cai, M. F., Tan, H. B., Chan, C. K., Qin, Y. M., Xu, H. B., Li, F., Schurman, M. I., Liu, L., and Zhao, J.: The size-resolved cloud condensation nuclei (CCN) activity and its prediction based on aerosol

hygroscopicity and composition in the Pearl Delta River (PRD) region during wintertime 2014, Atmos. Chem. Phys., 18, 16419-16437, doi:https://doi.org/10.5194/acp-18-16419-2018, 2018.

Chao, Q., Xiao, C., Li, w., Wang, L., Sun, L., Chen, X., Chen, Y., Li, Y., Gao, G., Liu, Y., Zhang, D., Ai, W., Chen, Y., Cui, T., Dai, T., Feng, A., Guo, Y., Huang, D., Jiang, Y., Li, D., Li, M., Liu, B., Liu, Y., Lv, Z., Mei, m., Wang, Q., Wang, Y., Yin, Y., Zeng, H., Zhang, Y., Zhai, J., Zhao, L., Zhi, R., Zhong, H., Zhou, X., Zhou, X., Zhu, X., and Wu, H.: China Climate Bulletin (2022), China Meteorological Administration, https://www.cma.gov.cn/zfxxgk/gknr/qxbg/202303/t20230324_5396394.html, 2022.

Choi, Y., Rhee, T. S., Collett, J. L., Park, T., Park, S.-M., Seo, B.-K., Park, G., Park, K., and Lee, T.: Aerosol concentrations and composition in the North Pacific marine boundary layer, Atmos Environ., 171, 165-172, doi:https://doi.org/10.1016/j.atmosenv.2017.09.047, 2017.

Crosbie, E., Youn, J. S., Balch, B., Wonaschutz, A., Shingler, T., Wang, Z., Conant, W. C., Betterton, E. A., and Sorooshian, A.: On the competition among aerosol number, size and composition in predicting CCN variability: a multi-annual field study in an urbanized desert, Atmos Chem Phys, 15, 6943-6958, doi:https://doi.org/10.5194/acp-15-6943-2015, 2015.

Deng, Z. Z., Zhao, C. S., Ma, N., Ran, L., Zhou, G. Q., Lu, D. R., and Zhou, X. J.: An examination of parameterizations for the CCN number concentration based on in situ measurements of aerosol activation properties in the North China Plain, Atmos. Chem. Phys., 13, 6227-6237, doi:https://doi.org/10.5194/acp-13-6227-2013, 2013.

Dusek, U., Frank, G. P., Hildebrandt, L., Curtius, J., Schneider, J., Walter, S., Chand, D., Drewnick, F., Hings, S., Jung, D., Borrmann, S., and Andreae, M. O.: Size matters more than chemistry for cloud-nucleating ability of aerosol particles, Science, 312, 1375-1378, doi:https://doi.org/10.1126/science.1125261, 2006.

Fitzgerald, J. W.: Dependence of the Supersaturation Spectrum of CCN on Aerosol Size Distribution and Composition, J Atmos Sci, 30, 628-634, doi:https://doi.org/10.1175/1520-0469(1973)030, 1973.

Fletcher, Squires, I. b. P., and Bowen, F. b. E. G.: The Physics of Rainclouds, 2011.

Geng, X. F., Zhong, G. C., Li, J., Cheng, Z. B., Mo, Y. Z., Mao, S. D., Su, T., Jiang, H. Y., Ni, K. W., and Zhang, G.: Molecular marker study of aerosols in the northern South China Sea: Impact of atmospheric outflow from the Indo-China Peninsula and South China, Atmos Environ, 206, 225-236, doi:https://doi.org/10.1016/j.atmosenv.2019.02.033, 2019.

566 Gras, J. L.: CN, CCN and particle size in Southern Ocean air at Cape Grim, Atmos Res, 35, 233-251,
567 doi:https://doi.org/10.1016/0169-8095(94)00021-5, 1995.
568 Gras, J. L. and Keywood, M.: Cloud condensation nuclei over the Southern Ocean: wind dependence
569 and seasonal cycles, Atmos. Chem. Phys., 17, 4419-4432, doi:https://doi.org/10.5194/acp-17-4419-2017,
570 2017.
571 Gysel, M., Crosier, J., Topping, D. O., Whitehead, J. D., Bower, K. N., Cubison, M. J., Williams, P. I.,
572 Flynn, M. J., McFiggans, G. B., and Coe, H.: Closure study between chemical composition and
573 hygroscopic growth of aerosol particles during TORCH2, Atmos. Chem. Phys., 7, 6131-6144,
574 doi:https://doi.org/10.5194/acp-7-6131-2007, 2007.
575 Huang, S., Wu, Z. J., Poulain, L., van Pinxteren, M., Merkel, M., Assmann, D., Herrmann, H., and
576 Wiedensohler, A.: Source apportionment of the organic aerosol over the Atlantic Ocean from 53 degrees
577 N to 53 degrees S: significant contributions from marine emissions and long-range transport, Atmos.
578 Chem. Phys., 18, 18043-18062,doi: 10.5194/acp-18-18043-2018, 2018
579 Huang, S., Wu, Z., Wang, Y., Poulain, L., Höpner, F., Merkel, M., Herrmann, H., and Wiedensohler, A.:
580 Aerosol Hygroscopicity and its Link to Chemical Composition in a Remote Marine Environment Based
581 on Three Transatlantic Measurements, Environ. Sci. Technol, 56, 9613-9622,
582 doi:https://doi.org/10.1021/acs.est.2c00785, 2022.
583 Ipcc: Annex I: Observational Products [Trewin, B. (ed.)], in: Climate Change 2021: The Physical Science
584 Basis. Contribution of Working Group I to the Sixth Assessment Report of the Intergovernmental Panel
585 on Climate Change, edited by: Masson-Delmotte, V., Zhai, P., Pirani, A., Connors, S. L., Péan, C., Berger,
586 S., Caud, N., Chen, Y., Goldfarb, L., Gomis, M. I., Huang, M., Leitzell, K., Lonnoy, E., Matthews, J. B.
587 R., Maycock, T. K., Waterfield, T., Yelekçi, O., Yu, R., and Zhou, B., Cambridge University Press,
588 Cambridge, United Kingdom and New York, NY, USA, 2061–2086,
589 https://doi.org/10.1017/9781009157896.015, 2021.
590 Jimenez, J. L., Canagaratna, M. R., Donahue, N. M., Prevot, A. S., Zhang, Q., Kroll, J. H., DeCarlo, P.
591 F., Allan, J. D., Coe, H., Ng, N. L., Aiken, A. C., Docherty, K. S., Ulbrich, I. M., Grieshop, A. P., Robinson,
592 A. L., Duplissy, J., Smith, J. D., Wilson, K. R., Lanz, V. A., Hueglin, C., Sun, Y. L., Tian, J., Laaksonen,
593 A., Raatikainen, T., Rautiainen, J., Vaattovaara, P., Ehn, M., Kulmala, M., Tomlinson, J. M., Collins, D.
594 R., Cubison, M. J., Dunlea, E. J., Huffman, J. A., Onasch, T. B., Alfarra, M. R., Williams, P. I., Bower,
595 K., Kondo, Y., Schneider, J., Drewnick, F., Borrmann, S., Weimer, S., Demerjian, K., Salcedo, D., Cottrell,

L., Griffin, R., Takami, A., Miyoshi, T., Hatakeyama, S., Shimono, A., Sun, J. Y., Zhang, Y. M., Dzepina, K., Kimmel, J. R., Sueper, D., Jayne, J. T., Herndon, S. C., Trimborn, A. M., Williams, L. R., Wood, E. C., Middlebrook, A. M., Kolb, C. E., Baltensperger, U., and Worsnop, D. R.: Evolution of organic aerosols in the atmosphere, Science, 326, 1525-1529, doi:https://doi.org/10.1126/science.1180353, 2009.

Kawana, K., Miyazaki, Y., Omori, Y., Tanimoto, H., Kagami, S., Suzuki, K., Yamashita, Y., Nishioka, J., Deng, Y. G., Yai, H., and Mochida, M.: Number-Size Distribution and CCN Activity of Atmospheric Aerosols in the Western North Pacific During Spring Pre-Bloom Period: Influences of Terrestrial and Marine Sources, J Geophys Res-Atmos, 127, e2022JD036690, doi:https://doi.org/10.1029/2022JD036690, 2022.

Köhler, H.: The nucleus in and the growth of hygroscopic droplets, Trans. Faraday Soc., 32, 1152-1161, doi:https://doi.org/10.1039/TF9363201152, 1936.

Lambe, A. T., Onasch, T. B., Massoli, P., Croasdale, D. R., Wright, J. P., Ahern, A. T., Williams, L. R., Worsnop, D. R., Brune, W. H., and Davidovits, P.: Laboratory studies of the chemical composition and cloud condensation nuclei (CCN) activity of secondary organic aerosol (SOA) and oxidized primary organic aerosol (OPOA), Atmos. Chem. Phys., 11, 8913-8928, doi:https://doi.org/10.5194/acp-11-8913-2011, 2011.

Lathem, T. L. and Nenes, A.: Water Vapor Depletion in the DMT Continuous-Flow CCN Chamber: Effects on Supersaturation and Droplet Growth, Aerosol Sci Tech, 45, 604-615, doi:https://doi.org/10.1080/02786826.2010.551146, 2011.

Leena, P. P., Pandithurai, G., Anilkumar, V., Murugavel, P., Sonbawne, S. M., and Dani, K. K.: Seasonal variability in aerosol, CCN and their relationship observed at a high altitude site in Western Ghats, Meteorol Atmos Phys, 128, 143-153, doi:https://doi.org/10.1007/s00703-015-0406-0, 2016.

Liang, B., Cai, M., Sun, Q., Zhou, S., and Zhao, J.: Source apportionment of marine atmospheric aerosols in northern South China Sea during summertime 2018, Environ. Pollut, 289, 117948, doi:https://doi.org/10.1016/j.envpol.2021.117948, 2021.

Liu, P., Song, M., Zhao, T., Gunthe, S. S., Ham, S., He, Y., Qin, Y. M., Gong, Z., Amorim, J. C., Bertram, A. K., and Martin, S. T.: Resolving the mechanisms of hygroscopic growth and cloud condensation nuclei activity for organic particulate matter, Nat. Commun, 9, 4076, doi:https://doi.org/10.1038/s41467-018-06622-2, 2018.

625 Liu, Y., Sun, L., Zhou, X., Luo, Y., Huang, W., Yang, C., Wang, Y., and Huang, T.: A 1400-year
626 terrigenous dust record on a coral island in South China Sea, Sci Rep, 4, 4994,
627 doi:https://doi.org/10.1038/srep04994, 2014.
628 Lu, W., Yang, S., Zhu, W., Li, X., Cui, S., Luo, T., Han, L., and Shi, J.: Evaluation of High Cloud Product
629 of ECMWF Over South China Sea Using CALIOP, Earth Space Sci, 9, e2021EA002113,
630 doi:https://doi.org/10.1029/2021ea002113, 2022.
631 Meng, J. W., Yeung, M. C., Li, Y. J., Lee, B. Y. L., and Chan, C. K.: Size-resolved cloud condensation
632 nuclei (CCN) activity and closure analysis at the HKUST Supersite in Hong Kong, Atmos. Chem. Phys.,
633 14, 10267-10282, doi:https://doi.org/10.5194/acp-14-10267-2014, 2014.
634 Moore, R. H., Nenes, A., and Medina, J.: Scanning Mobility CCN Analysis-A Method for Fast
635 Measurements of Size-Resolved CCN Distributions and Activation Kinetics, Aerosol Sci Tech, 44, 861-
636 871, doi:https://doi.org/10.1080/02786826.2010.498715, 2010.
637 Ou, H., Cai, M., Zhang, Y., Ni, X., Liang, B., Sun, Q., Mai, S., Sun, C., Zhou, S., Wang, H., Sun, j., and
638 Zhao, J.: Measurement Report: Seasonal variation and anthropogenic influence on cloud condensation
639 nuclei (CCN) activity in the South China Sea: Insights from shipborne observations during summer and
640 winter of 2021 [dataset], doi:https://doi.org/10.6084/m9.figshare.25472545, 2024.
641 Ovadnevaite, J., Zuend, A., Laaksonen, A., Sanchez, K. J., Roberts, G., Ceburnis, D., Decesari, S.,
642 Rinaldi, M., Hodas, N., Facchini, M. C., Seinfeld, J. H., and O' Dowd, C.: Surface tension prevails over
643 solute effect in organic-influenced cloud droplet activation, Nature, 546, 637-641,
644 doi:https://doi.org/10.1038/nature22806, 2017.
645 Park, M., Yum, S. S., Kim, N., Cha, J. W., Shin, B., and Ryoo, S.-B.: Characterization of submicron
646 aerosols and CCN over the Yellow Sea measured onboard the Gisang 1 research vessel using the positive
647 matrix factorization analysis method, Atmos Res, 214, 430-441,
648 doi:https://doi.org/10.1016/j.atmosres.2018.08.015, 2018.
649 Patel, P. N. and Jiang, J. H.: Cloud condensation nuclei characteristics at the Southern Great Plains site:
650 role of particle size distribution and aerosol hygroscopicity, Environ Res Commun, 3,
651 doi:https://doi.org/10.1088/2515-7620/ac0e0b, 2021
652 Petters, M. D. and Kreidenweis, S. M.: A single parameter representation of hygroscopic growth and
653 cloud condensation nucleus activity, Atmos. Chem. Phys., 7, 1961-1971, doi:https://doi.org/10.5194/acp-
654 7-1961-2007, 2007.

Pöhlker, M. L., Pöhlker, C., Ditas, F., Klimach, T., Hrabe de Angelis, I., Araújo, A., Brito, J., Carbone, S., Cheng, Y., Chi, X., Ditz, R., Gunthe, S. S., Kesselmeier, J., Könemann, T., Lavrič, J. V., Martin, S. T., Mikhailov, E., Moran-Zuloaga, D., Rose, D., Saturno, J., Su, H., Thalman, R., Walter, D., Wang, J., Wolff, S., Barbosa, H. M. J., Artaxo, P., Andreae, M. O., and Pöschl, U.: Long-term observations of cloud condensation nuclei in the Amazon rain forest – Part 1: Aerosol size distribution, hygroscopicity, and new model parametrizations for CCN prediction, Atmos. Chem. Phys., 16, 15709-15740, doi:https://doi.org/10.5194/acp-16-15709-2016, 2016.

Qin, Y., Wang, H., Wang, Y., Lu, X., Tang, H., Zhang, J., Li, L., and Fan, S.: Wildfires in Southeast Asia pollute the atmosphere in the northern South China Sea, Sci Bull (Beijing), 69, 1011-1015, doi:https://doi.org/10.1016/j.scib.2024.02.026, 2024.

Quinn, P. K., Bates, T. S., Coffman, D. J., and Covert, D. S.: Influence of particle size and chemistry on the cloud nucleating properties of aerosols, Atmos. Chem. Phys., 8, 1029-1042, doi:https://doi.org/10.5194/acp-8-1029-2008, 2008.

Quinn, P. K., Bates, T. S., Coffman, D. J., Upchurch, L., Johnson, J. E., Moore, R., Ziemba, L., Bell, T. G., Saltzman, E. S., Graff, J., and Behrenfeld, M. J.: Seasonal Variations in Western North Atlantic Remote Marine Aerosol Properties, J Geophys Res-Atmos, 124, 14240-14261, doi:https://doi.org/10.1029/2019jd031740, 2019.

Rose, D., Nowak, A., Achtert, P., Wiedensohler, A., Hu, M., Shao, M., Zhang, Y., Andreae, M. O., and Poschl, U.: Cloud condensation nuclei in polluted air and biomass burning smoke near the mega-city Guangzhou, China - Part 1: Size-resolved measurements and implications for the modeling of aerosol particle hygroscopicity and CCN activity, Atmos. Chem. Phys., 10, 3365-3383, doi:https://doi.org/10.5194/acp-10-3365-2010, 2010.

Ross, K. E., Piketh, S. J., Bruintjes, R. T., Burger, R. P., Swap, R. J., and Annegarn, H. J.: Spatial and seasonal variations in CCN distribution and the aerosol-CCN relationship over southern Africa, J Geophys Res-Atmos, 108, doi:https://doi.org/10.1029/2002jd002384, 2003.

Sarangi, B., Ramachandran, S., Rajesh, T. A., and Dhaker, V. K.: Black carbon linked aerosol hygroscopic growth: Size and mixing state are crucial, Atmos Environ., 200, 110-118, doi:https://doi.org/https://doi.org/10.1016/j.atmosenv.2018.12.001, 2019.

Schmale, J., Henning, S., Decesari, S., Henzing, B., Keskinen, H., Sellegri, K., Ovadnevaite, J., Pohlker, M. L., Brito, J., Bougiatioti, A., Kristensson, A., Kalivitis, N., Stavroulas, I., Carbone, S., Jefferson, A.,

Park, M., Schlag, P., Iwamoto, Y., Aalto, P., Aijala, M., Bukowiecki, N., Ehn, M., Frank, G., Frohlich, R., Frumau, A., Herrmann, E., Herrmann, H., Holzinger, R., Kos, G., Kulmala, M., Mihalopoulos, N., Nenes, A., O'Dowd, C., Petaja, T., Picard, D., Pohlker, C., Poschl, U., Poulain, L., Prevot, A. S. H., Swietlicki, E., Andreae, M. O., Artaxo, P., Wiedensohler, A., Ogren, J., Matsuki, A., Yum, S. S., Stratmann, F., Baltensperger, U., and Gysel, M.: Long-term cloud condensation nuclei number concentration, particle number size distribution and chemical composition measurements at regionally representative observatories, Atmos. Chem. Phys., 18, 2853-2881, doi:https://doi.org/10.5194/acp-18-2853-2018, 2018.

Seinfeld, J. H. and Pandis, S. N.: Atmospheric Chemistry and Physics: From Air Pollution to Climate Change, Wiley2016.

Sihto, S. L., Mikkila, J., Vanhanen, J., Ehn, M., Liao, L., Lehtipalo, K., Aalto, P. P., Duplissy, J., Petaja, T., Kerminen, V. M., Boy, M., and Kulmala, M.: Seasonal variation of CCN concentrations and aerosol activation properties in boreal forest, Atmos. Chem. Phys., 11, 13269-13285, doi:https://doi.org/10.5194/acp-11-13269-2011, 2011.

Sun, Q., Liang, B., Cai, M., Zhang, Y., Ou, H., Ni, X., Sun, X., Han, B., Deng, X., Zhou, S., and Zhao, J.: Cruise observation of the marine atmosphere and ship emissions in South China Sea: Aerosol composition, sources, and the aging process, Environ. Pollut, 316, 120539, doi:https://doi.org/10.1016/j.envpol.2022.120539, 2023.

Wang, B., Huang, F., Wu, Z., Yang, J., Fu, X., and Kikuchi, K.: Multi-scale climate variability of the South China Sea monsoon: A review, Dynam Atmos Oceans, 47, 15-37, doi:https://doi.org/10.1016/j.dynatmoce.2008.09.004, 2009.

Wang, Y. Q.: MeteoInfo: GIS software for meteorological data visualization and analysis, Meteorol. Appl, 21, 360-368, doi:https://doi.org/10.1002/met.1345, 2014.

Xiao, H.-W., Xiao, H.-Y., Luo, L., Shen, C.-Y., Long, A.-M., Chen, L., Long, Z.-H., and Li, D.-N.: Atmospheric aerosol compositions over the South China Sea: temporal variability and source apportionment, Atmos. Chem. Phys., 17, 3199-3214, doi:https://doi.org/10.5194/acp-17-3199-2017, 2017.

711 Table 1. The number concentration of particle and cloud condensation nuclei at different supersaturation (SS), the hygroscopicity and bulk activation ratio (AR), and activation

712 diameter (D_{50}) at different SS in different studies.

Location	period	N_{CN} (cm^{-3})	N_{CCN} (cm^{-3})	Hygroscopicity (κ)	Bulk AR	D_{50} (nm)	Reference
South China Sea	2021.05.05-2021.06.09	6966±9249	2640±3639 (0.20% SS) 4392±6415 (0.40% SS) 5215±6862 (0.70% SS)	0.47±0.21 (0.20% SS) 0.54±0.21 (0.40% SS)	0.37±0.16 (0.20% SS) 0.63±0.17 (0.40% SS) 0.87±0.17 (0.70% SS)	96±19 (0.20% SS) 57±9 (0.40% SS)	This study
Northern South China Sea	2021.12.19-2021.12.29	4988±3474	1086±691 (0.10% SS) 1625±1110 (0.20% SS) 2218±1503 (0.40% SS) 2797±1883 (0.70% SS)	0.50±0.21 (0.10% SS) 0.31±0.10 (0.20% SS) 0.19±0.05 (0.40% SS) 0.15±0.05 (0.70% SS)	0.23±0.09 (0.10% SS) 0.33±0.12 (0.20% SS) 0.44±0.13 (0.40% SS) 0.55±0.14 (0.70% SS)	145±18 (0.10% SS) 107±13 (0.20% SS) 79±7 (0.40 % SS) 59±6 (0.70% SS)	This study
Northern South China Sea	2018.08.06-2018.08.27	3463	1544 (0.34% SS)	0.38±0.09 (0.18% SS) 0.40±0.08 (0.34% SS) 0.38±0.08 (0.59% SS)	/	/	Cai et al., 2020
Remote South China Sea	2012.09.14-2012.09.26	503±455	450±388 (0.14% SS) 675±516 (0.38% SS) 698±555 (0.53% SS) 724±512 (0.71% SS)	0.54±0.14 (0.14% SS) 0.50±0.21 (0.38% SS)	0.47±0.16 (0.14% SS) 0.72±0.17 (0.38% SS) 0.79±0.15 (0.53% SS) 0.85±0.13 (0.71% SS)	/	Atwood et al., 2017
Western North Pacific	2015.03.04-2015.03.26	/	/	0.75±0.21 (0.11% SS) 0.51±0.16 (0.24% SS) 0.45±0.16 (0.60% SS)	0.40±0.22 (0.11% SS) 0.50±0.22 (0.24% SS) 0.70±0.23 (0.60% SS)	/	Kawana et al., 2020
Guangzhou	2014.11-2014.12	/	3103±1913 (0.10% SS) 5095±2972 (0.20% SS) 6524±3783 (0.40% SS)	0.37±0.11 (0.10% SS) 0.29±0.09 (0.20% SS) 0.18±0.07 (0.40% SS)	0.26±0.10 (0.10% SS) 0.41±0.14 (0.20% SS) 0.53±0.15 (0.40% SS)	156 ± 19 (0.1% SS) 107 ± 17 (0.2% SS) 78 ± 15 (0.4% SS)	Cai et al., 2018

			7913±4234 (0.70% SS)	0.15±0.06 (0.70% SS)	0.64±0.13 (0.70% SS)	58 ± 11 (0.7% SS)	
Yellow Sea	2017.04-2017.05	7622±4038	4821±1763 (0.63% SS)	/	/	/	Park et al., 2018

713

714 Table 2. The number concentration of particle, cloud condensation nuclei, and bulk activation ratio in
715 different periods.

	Summer			Winter		
Cluster	Indochinese Peninsula	Luzon	Marine	Mainland China	Marine	Mixed
N_{CCN} (cm^{-3})						
0.1% SS	\	\	\	1359±669	439±223	945±400
0.2% SS	1200±787	4066±4748	1135±800	2058±1095	614±318	1460±514
0.4% SS	1650±1187	7804±8608	1812±1052	2792±1478	830±424	1801±640
0.7% SS	2239±1367	10480±9741	2515±1523	3514±1841	1024±463	2101±757
N_{CN} (cm^{-3})						
Total	2699±2147	14674±13844	3033±2366	6875±3263	1728±465	2918±1204
Nucleation	111±206	1543±3341	238±426	893±925	214±281	141±191
Aikten	1156±1261	8653±8815	1668±1526	3089±2017	732±337	806±427
Accumulation	1434±1444	3764±4157	1121±929	2923±2440	781±313	1975±831
Bulk AR						
0.1% SS	\	\	\	0.21±0.07	0.26±0.10	0.32±0.04
0.2% SS	0.49±0.13	0.31±0.17	0.40±0.13	0.30±0.09	0.36±0.14	0.51±0.05
0.4% SS	0.73±0.09	0.55±0.18	0.68±0.14	0.40±0.10	0.49±0.16	0.63±0.06
0.7% SS	0.98±0.15	0.76±0.16	0.90±0.13	0.50±0.09	0.61±0.18	0.73±0.06

716

717

718 Table 3. The slope and coefficient of determination (in parentheses) in CCN closure analysis at
719 different supersaturations in different periods.

	Summer			Winter		
Cluster	Luzon	Indochinese Peninsula	Marine	Mainland China	Mixed	Marine
Internal scheme						
0.1% SS	\	\	\	0.91 (0.97)	0.72 (0.95)	0.71 (0.94)
0.2% SS	0.83 (0.89)	0.89 (0.81)	0.76 (0.96)	1.13 (0.96)	1.01 (0.99)	0.94 (0.97)
0.4% SS	0.90 (0.96)	0.90 (0.98)	0.89 (0.97)	1.34 (0.97)	1.14 (0.98)	1.04 (0.98)
0.7% SS	0.91 (0.93)	0.96 (0.92)	0.88 (0.98)	1.38 (0.97)	1.16 (0.99)	1.04 (0.96)
External scheme						
0.1% SS	\	\	\	0.80 (0.97)	0.62 (0.95)	0.59 (0.94)
0.2% SS	0.74 (0.88)	0.77 (0.79)	0.80 (0.96)	1.01 (0.97)	0.90 (0.99)	0.81 (0.97)
0.4% SS	0.78 (0.93)	0.80 (0.97)	0.82 (0.96)	1.23 (0.97)	1.05 (0.98)	0.95 (0.98)
0.7% SS	0.80 (0.92)	0.89 (0.92)	0.80 (0.98)	1.24 (0.98)	1.11 (0.99)	1.00 (0.96)

720
721

722 FIGURE CAPTION

723 Figure 1. The cruises of two shipborne observations, and the location of sample line and chimney of Tan
724 Kah Kee, and Sun Yat-sen scientific vessel (a); Wind rose of the wind direction and wind speed in
725 summer and winter cruises; The radius represents the frequency of wind direction occurrences, and the
726 shaded areas indicate wind speed (b) and (c). The red circles are the midpoints of the ship trajectory
727 selected for backward trajectory and cluster analysis in summer and the orange squares are the midpoints
728 of the ship trajectory selected for backward trajectory and cluster analysis in winter.

729 Figure 2. Timeseries of (a) particle number size distribution, (b) mass concentration of NR-PM_1, and (c)
730 its fraction, (d) mass concentration of organic carbon and elemental carbon, (e) number concentration of
731 total particle and cloud condensation nuclei under the supersaturation of 0.1%, 0.2%, 0.4%, and 0.7%,
732 and (f) aerosol hygroscopicity. The number 1 in figure number means timeseries in summer and number
733 2 means it in winter.

734 Figure 3. Particle number size distribution in summer (a) and winter (b); The red markers represent the
735 activation diameters and hygroscopicity parameters corresponding to 0.1%, 0.2%, 0.4%, and 0.7%
736 supersaturations in this study (without 0.1% in summer). The green markers represent the hygroscopicity
737 parameters reported in Atwood et al. (2017) for the southern South China Sea during summer. The gray
738 markers represent the hygroscopicity parameters documented in Cai et al. (2018) for the Pearl River
739 Delta region during winter. The fraction of NR-PM_1 in summer (c) and winter (d) in this study, in northern
740 SCS reported by Liang et al. (2021) (e), and in North Pacific reported by Choi et al. (2017) (f).

741 Figure 4. The cluster analysis result in summer (a) and winter (b). The solid line in summer means cluster
742 analysis from May 5 to May 24 and the dash line in summer means cluster analysis from May 25 to June
743 9; The solid line in winter means cluster analysis from Dec 19 to Dec 21 and Dec 27 to Dec 29, and the
744 dash line in winter means cluster analysis from Dec 22 to Dec 26.

745 Figure 5. The fraction of NR-PM_1 in “Luzon” period (a), “Indochinese Peninsula" period (b), and
746 “Marine-s” period (c) in summer. The fraction of NR-PM_1 in “Mainland China” period (d), “Mixed"
747 period (e), and “Marine-w” period (f) in winter.

748 Figure 6. The particle number size distribution (PNSD) in “Luzon” period (a), “Indochinese Peninsula"
749 period (b), and “Marine-s” period (c) in summer. The PNSD in “Mainland China” period (d), “Mixed"
750 period (e), and “Marine-w” period (f) in winter.

751 Figure 7. The bulk activation ratio (AR) at different supersaturation (SS) in different periods (a); The
752 aerosol hygroscopicity (κ) at different supersaturation (SS) in different periods (b).
753 Figure 8. The normalized mean bias (NMB) calculated by “Internal-mixed” scheme and “External-mixed”
754 scheme according to CCN closure method. The marker of circle means “Internal-mixed” scheme and the
755 marker of triangle means “External-mixed” scheme. Different colors means different supersaturations.
756

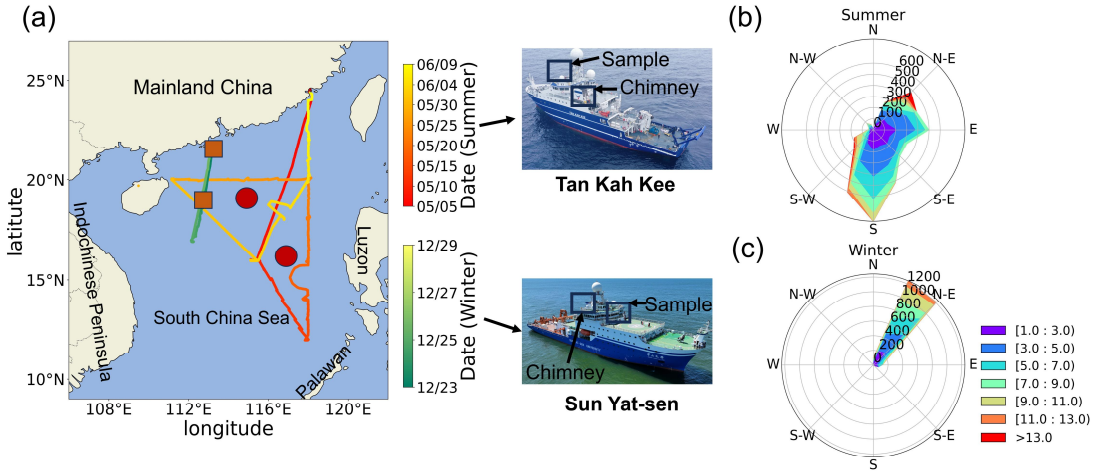
(a)
Mainland China
South China Sea
Indochinese Peninsula
Luzon
Palawan
25°N
20°N
15°N
10°N
latitute
108°E
112°E
116°E
120°E
longitude
06/09
06/04
05/30
05/25
05/20
05/15
05/10
05/05
Date (Summer)
12/29
12/27
12/25
12/23
Date (Winter)
Sample
Chimney
Tan Kah Kee
Sample
Chimney
Sun Yat-sen
(b)
Summer
N
N-E
E
S-E
S
S-W
W
N-W
600
500
400
300
200
100
0
(c)
Winter
1200
1000
800
600
400
200
[1.0 : 3.0)
[3.0 : 5.0)
[5.0 : 7.0)
[7.0 : 9.0)
[9.0 : 11.0)
[11.0 : 13.0)
>13.0

Fig. 1

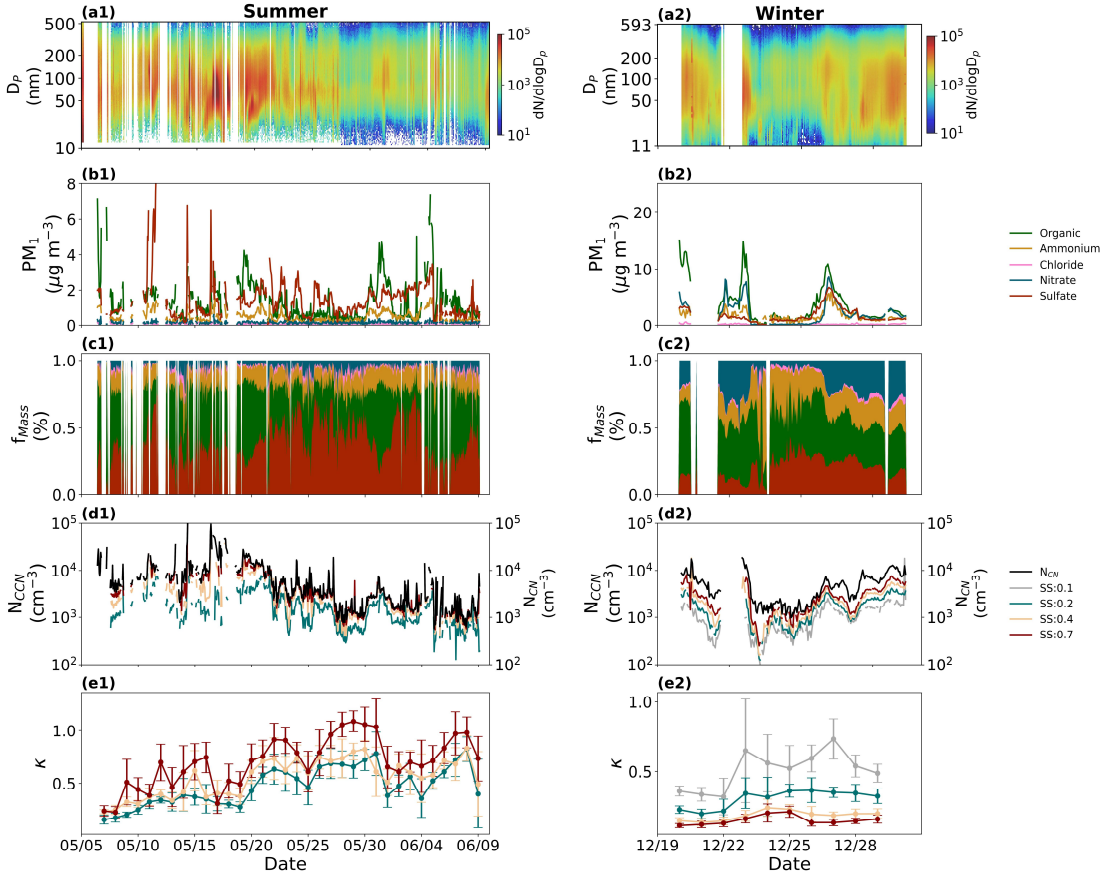
(a1)
Summer
(a2)
Winter
D_P (nm)
dN/dlogD_p
(b1)
(b2)
PM_1 ($\mu g\ m^{-3}$)
Organic
Ammonium
Chloride
Nitrate
Sulfate
(c1)
(c2)
f_{Mass} (%)
(d1)
(d2)
N_{CCN} (cm^{-3})
N_{CN} (cm^{-3})
SS:0.1
SS:0.2
SS:0.4
SS:0.7
(e1)
(e2)
κ
05/05 05/10 05/15 05/20 05/25 05/30 06/04 06/09
12/19 12/22 12/25 12/28
Date

Fig. 2

766

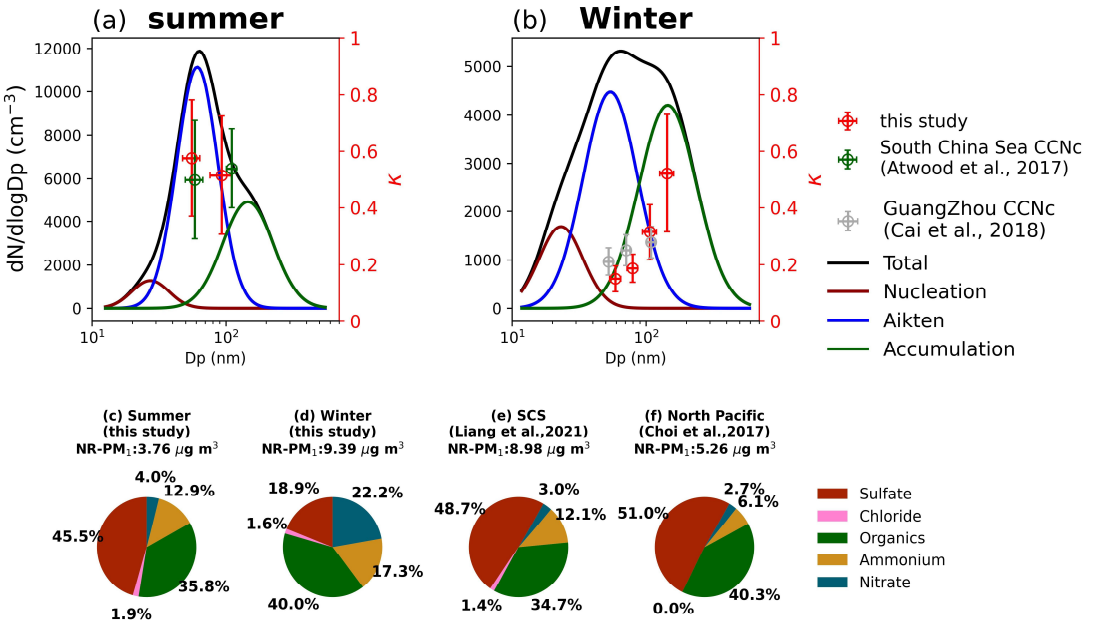

767

768 Fig. 3

769

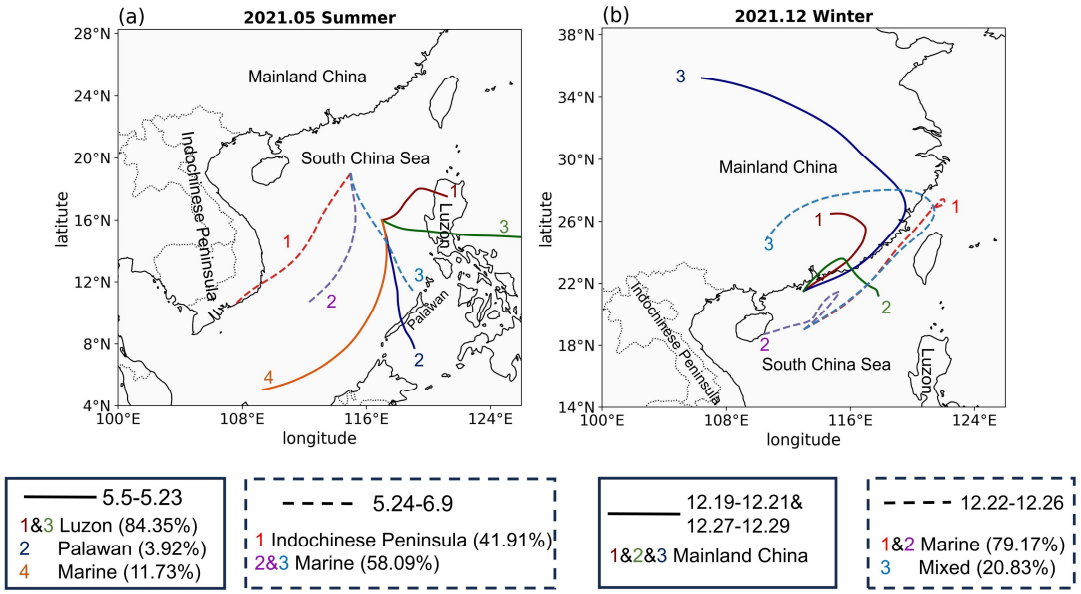

770

771 Fig. 4

772

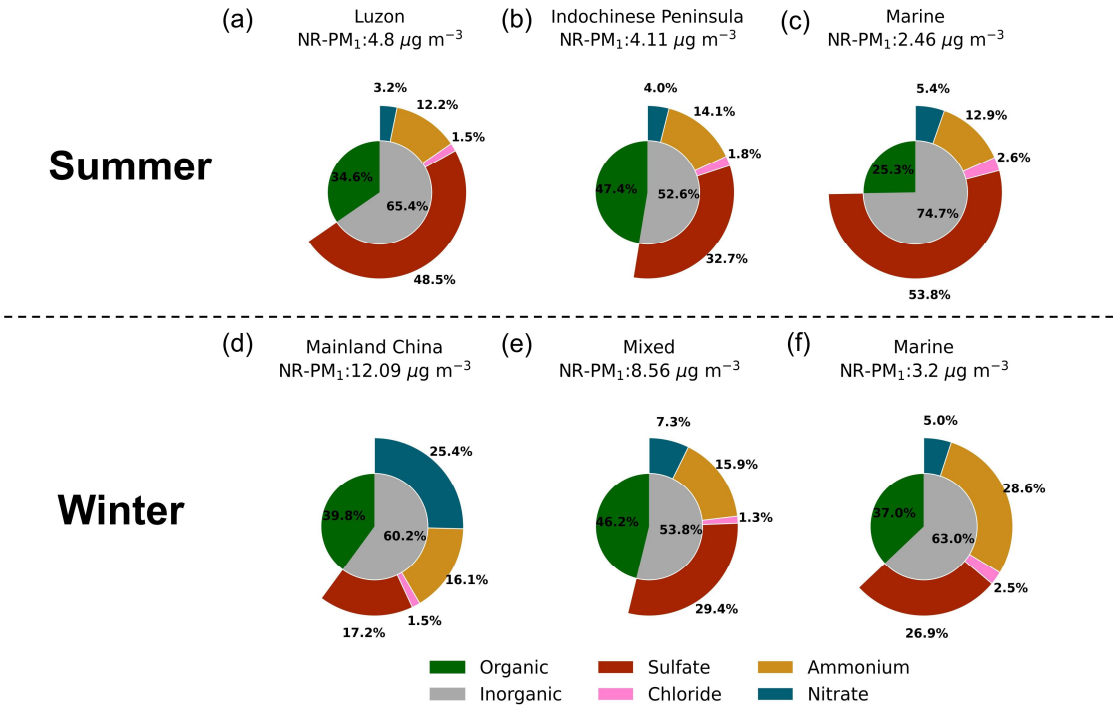
(a) Luzon
NR-PM1:4.8 μg m−3
(b) Indochinese Peninsula
NR-PM1:4.11 μg m−3
(c) Marine
NR-PM1:2.46 μg m−3
Summer
3.2%
12.2%
1.5%
34.6%
65.4%
48.5%
4.0%
14.1%
1.8%
47.4%
52.6%
32.7%
5.4%
12.9%
2.6%
25.3%
74.7%
53.8%
(d) Mainland China
NR-PM1:12.09 μg m−3
(e) Mixed
NR-PM1:8.56 μg m−3
(f) Marine
NR-PM1:3.2 μg m−3
Winter
25.4%
39.8%
60.2%
16.1%
1.5%
17.2%
7.3%
15.9%
46.2%
53.8%
1.3%
29.4%
5.0%
28.6%
37.0%
63.0%
2.5%
26.9%
Organic
Inorganic
Sulfate
Chloride
Ammonium
Nitrate

Fig.5

777

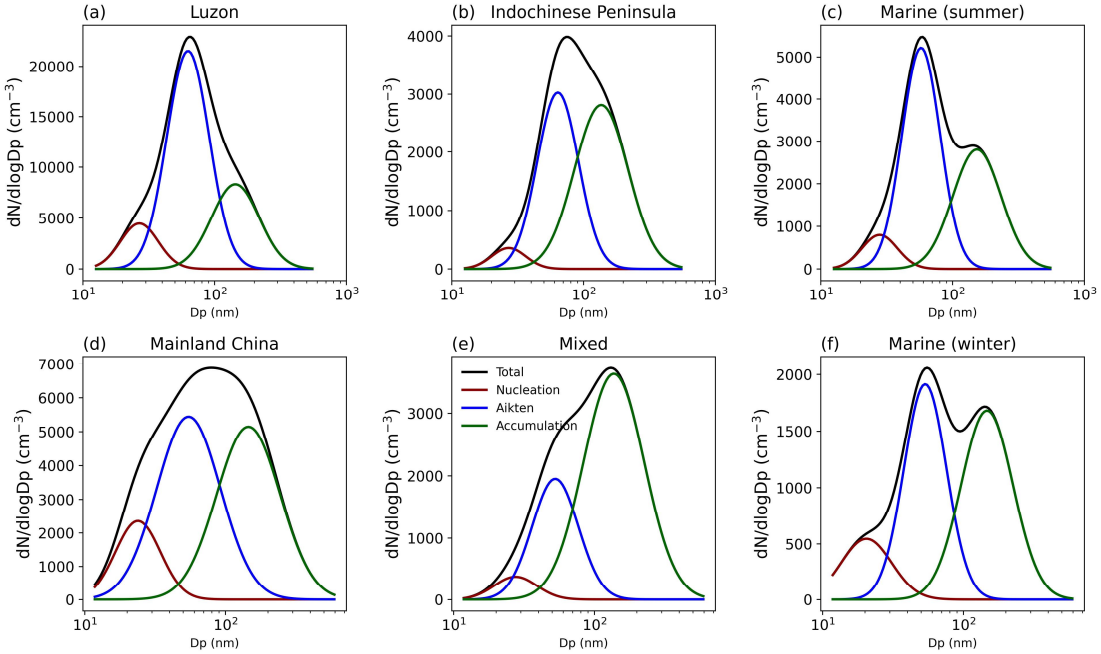

778

779 Fig. 6

780

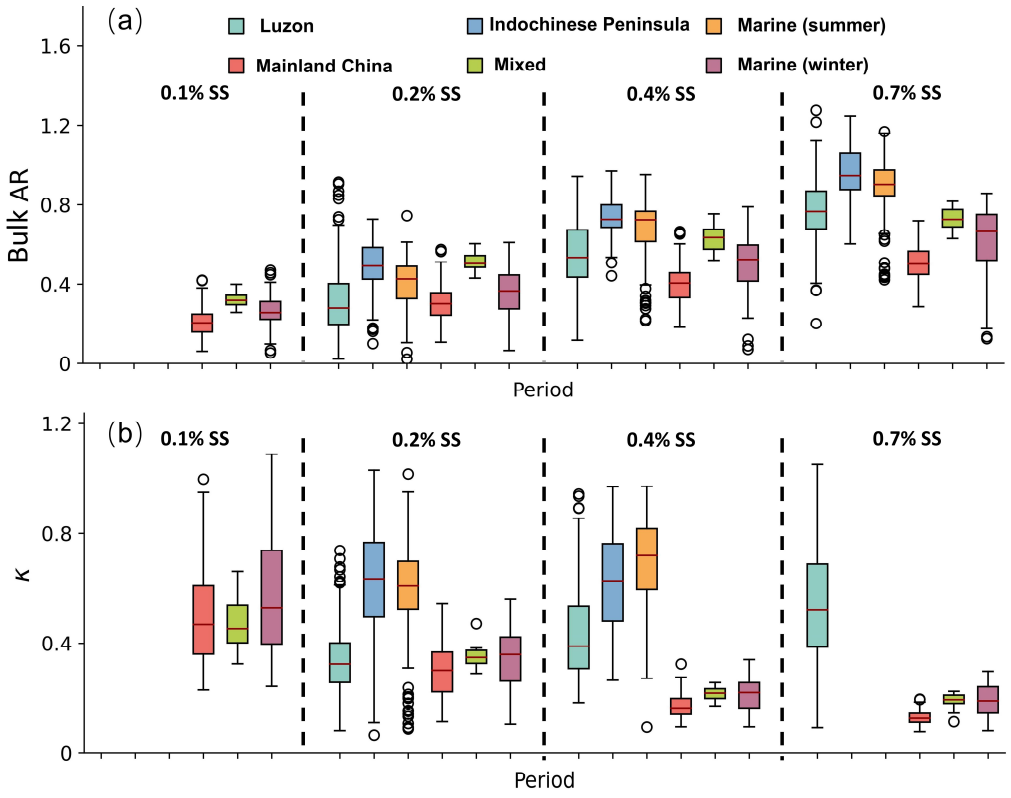
(a)
Luzon
Indochinese Peninsula
Marine (summer)
Mainland China
Mixed
Marine (winter)
0.1% SS
0.2% SS
0.4% SS
0.7% SS
Bulk AR
1.6
1.2
0.8
0.4
0
Period
(b)
0.1% SS
0.2% SS
0.4% SS
0.7% SS
κ
1.2
0.8
0.4
0
Period

Fig. 7

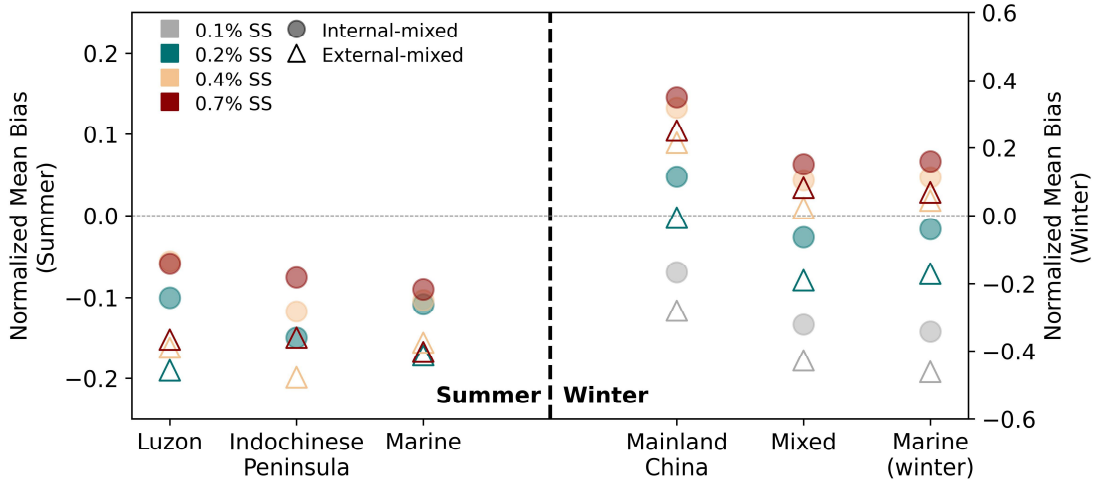
0.1% SS
0.2% SS
0.4% SS
0.7% SS
Internal-mixed
External-mixed
Normalized Mean Bias (Summer)
Normalized Mean Bias (Winter)
0.2
0.1
0.0
−0.1
−0.2
0.6
0.4
0.2
0.0
−0.2
−0.4
−0.6
Summer
Winter
Luzon
Indochinese Peninsula
Marine
Mainland China
Mixed
Marine (winter)

785

786 Fig. 8